



Cross-Scale Flow Field Analysis of Sealing Chamber and End Face Considering the CO₂ Real Gas Effect

X. J. Sun^{1,2}, P. Y. Song^{2†}, X. P. Hu³, W. Y. Mao², Q. G. Deng¹ and H. J. Xu²

¹ Faculty of Mechanical and Electrical Engineering, Kunming University of Science and Technology, Kunming, Yunnan, 650000, China

² Faculty of Chemical Engineering, Kunming University of Science and Technology, Kunming, Yunnan, 650000, China

³ Industrial Ecology Programme, Department of Energy and Process Engineering, Norwegian University of Science and Technology, Trondheim, 7491, Norway

†Corresponding Author Email: songpengyunkm@sina.com

(Received July 20, 2020; accepted November 20, 2020)

ABSTRACT

The dry gas seal (DGS) is a non-contacting, gas-lubricated mechanical face seal commonly used in rotating machinery. Traditional analyses of DGSs treat the end face as an independent factor by setting the end-face inlet as boundary conditions, but limited attention is focused on the sealing chamber of the DGS. Using the finite volume method and the shear stress transport (SST) $k-\omega$ model, the coupling between the millimeter-scale sealing chamber and the micrometer-scale end face are simulated with regard to the real gas effect of CO₂. The three-dimensional distributions of velocity, pressure and temperature in the cross-scale flow field are investigated under different working conditions. Moreover, the boundary parameters of the end-face inlet are modified by response surface methodology with a central composite rotatable design. The results demonstrate that the real gas effect of CO₂ leads to an increased total inlet flow. When the pressure reaches 10.3 MPa, the relative difference is 51.90% compared to ideal gas. Minor temperature and pressure changes occur in the sealing chamber when the dry gas seal is in operation. However, the inlet temperature of the end face T_f increases and the inlet pressure of the end face p_f decreases. These research results provide a reliable reference for engineering practice.

Keywords: Dry gas seal; Real gas effect; Sealing chamber; Numerical research; Response surface methodology.

NOMENCLATURE

a, b	R-K equation coefficient	a_2, a_5	sealing chamber inlet radius/diameter
ρ	gas density	a_3	rota ring ring thickness
U	speed vector	a_4	mating ring thickness
T	gas temperature	r_o	seal ring outer radius
μ	gas viscosity	r_g	seal ring groove inner dam radius
c_p	heat capacity at constant pressure	r_i	seal ring inner radius
κ	thermal conductivity	h	gas film thickness
S_T	thermal energy converted in viscous shear	N_g	number of spiral groove
R	gas constant	h_g	spiral depth
V	gas molar volume	α	spiral angle
T_c	critical temperature	g	land-to-groove ratio
P_c	critical pressure	p_i	inlet pressure
v	linear speed of rotation	p_o	outlet pressure
h_t	convective heat transfer coefficient	T_i	inlet temperature
R_1, R_2	sealing chamber inner/outer radius	T_o	outlet temperature
Z_f	compression factor	n	shaft rotation speed
a_1	sealing chamber axial length	p_f	inlet pressure of end face
		T_f	inlet temperature of end face

1. INTRODUCTION

A dry gas seal (DGS) is a non-contacting, gas-lubricated mechanical face seal commonly used in rotating machinery, such as compressors and centrifuges. Many studies address the DGS's end face, (Chen *et al.* 2018; Wang *et al.* 2019; Chen *et al.* 2019) but limited attention is focused on the sealing chamber. The gas flow state in the sealing chamber and the end face affect each other. Most analyses on the performance of the DGS treat the end face as an independent factor by setting the inlet temperature of the end face T_f and inlet pressure of the end face p_f as boundary conditions. (Xie *et al.* 2020; Meng and Khonsari 2018; Xu *et al.* 2019) However, there is no clear method to determine this boundary condition. For the dry gas seal, it is vital to analyze sealing performance and determine the boundary condition of the end-face inlet considering the gas flow effect in the sealing chamber. (Wang *et al.* 2018; Du *et al.* 2020)

The DGS, using CO₂ as a lubricant (CO₂ DGS), has developed rapidly in recent years and is widely used. However, the critical temperature and pressure of CO₂ are relatively low, and the critical state is easily reached during typical operating conditions, and even in a supercritical state. The characteristics of CO₂ deviate significantly from an ideal gas, and therefore, some scholars have investigated the real gas effect (RGE) of CO₂ on DGS. Thatte and Dheeradhada (2016) formulated a multi-scale physical model of DGS for supercritical carbon dioxide (sCO₂) turbines, and they added the real gas state equation to capture the sudden change in the physical parameters of fluid near the critical point. Their results demonstrated that high pressure and speed changed the density of the sCO₂ gas film. Consequently, the density change in turn affected the leakage rate, the local Mach number in the gas film, and further affects the local flow velocity in the gas film to reach the speed of sound. Using Fluent software, Fairuz and Jahn (2016, 2019) employed the Span and Wagner state equation to express the RGE of CO₂ using simulations with the DGS operating state in different working conditions. They determined that the RGE was significant when operating condition is close to the critical state of CO₂. However, the results of sCO₂ operating further from the critical state were similar to those of the ideal gas. For the largest gap operation, as the speed increased, the inertia effect increased, but the leakage rate of DGS decreased significantly. Du *et al.* (2018) established a thermo-fluid-solid coupling model of the rotating ring, primary ring, and the gas film, and they analysed the pressure and temperature differences, the opening force, and leakage rate with air and CO₂ as the sealing mediums. They determined that all the above-mentioned parameters increased significantly when the inlet temperature increased. Furthermore, the pressure difference, opening force, and leakage of the CO₂ model increased slightly more rapidly than the air model, while the increase of temperature difference was lower than in the air model. Xu *et al.* (2018) established a steady-state model of the spiral groove dry gas seal (S-DGS)

which considered the RGE and inertia effect. The RGE of CO₂ was expressed through the Viry equation. Their research investigated the influence of the steady-state performance on the pump-in model and the pump-out model (Song and Ding 2011) However, these studies did not consider the gas-flow effect of the sealing chamber on the sealing performance.

For this research, the Redlich-Kwong (RK) equation is selected to express the RGE of CO₂ by comparing various gas state equations, and the physical parameters of CO₂ are considered throughout the process (the physical parameters of CO₂ cross the critical point in this process). The double-face S-DGS is the research object. Fig. 1 shows the structure of S-DGS. Using the finite volume method and the shear stress transport (SST) $k-\omega$ model, the coupling between the millimeter-scale sealing chamber and the micrometer-scale end face are simulated. The flow characteristics, such as temperature, pressure, and flow rate of sealing gas, are analysed under different working conditions. The response surface methodology with a central composite rotatable design was further used to investigate the relationships between the operating parameters of the sealing chamber inlet and T_f and p_f . Thus, the influence of the sealing chamber on the expression of the end-face inlet is determined.

2. MODEL DESCRIPTION AND METHOD

2.1 Physical Model

The double-face S-DGS is periodically symmetrical, so only one-half of the model is selected for analysis. Due to the location of the gas inlet, smaller divisions are not practical. Figure 2 presents the physical model.

2.2 Basic Assumptions

The following assumptions are made for the sealing chamber and the gas film when DGS is in steady operation (Li 2007): (1) The boundary of the sealing chamber and the sealing rings are rigid materials. Therefore, the force deformation and thermal deformation are ignored; (2) The gas does not slip on the surface of the sealing chamber and the seal rings; (3) The effects of the roughness of sealing chamber surface and seal rings surface are ignored; (4) The rotating ring and primary ring are strictly aligned and the effects of disturbance and deflection are ignored.

2.3 Fluid Governing Equations

The gas medium is the CO₂ real gas, and the heat is mainly due to the viscous shear of the gas. Therefore, the governing equations in this research include mass, momentum, and energy conservation (Wang 2004). The S-DGS gas flow is in a steady state, so the change in density over time is negligible. The continuity equation can be expressed as follows:

$$\frac{\partial(\rho \cdot u_i)}{\partial x_i} = 0 \quad (1)$$

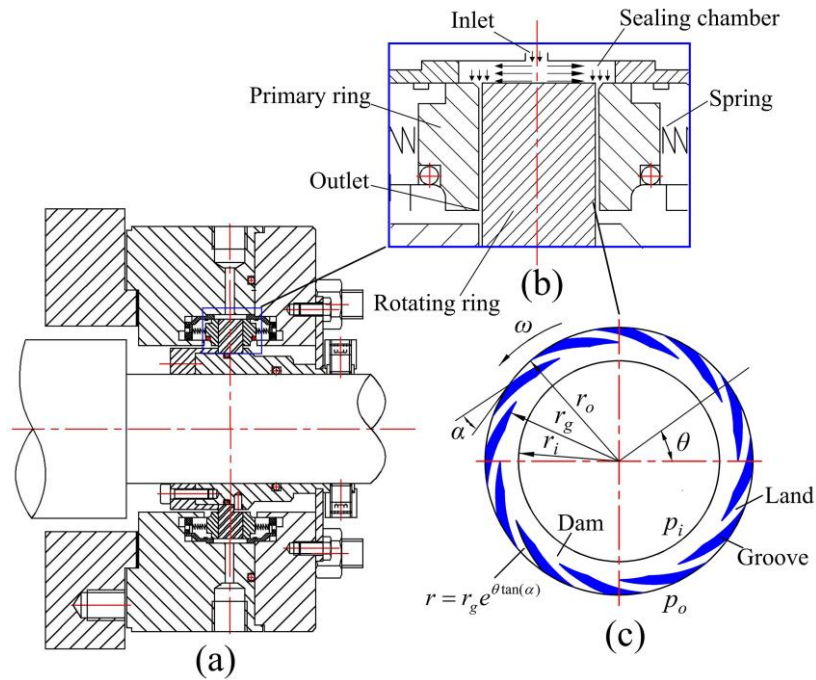


Fig. 1. Schematic diagram of the double-face DGS. (a) The holistic structure of the double-face DGS used for the pump. (b) The double-face sealing chamber of the section structure. (c) The end face of the spiral groove DGS.

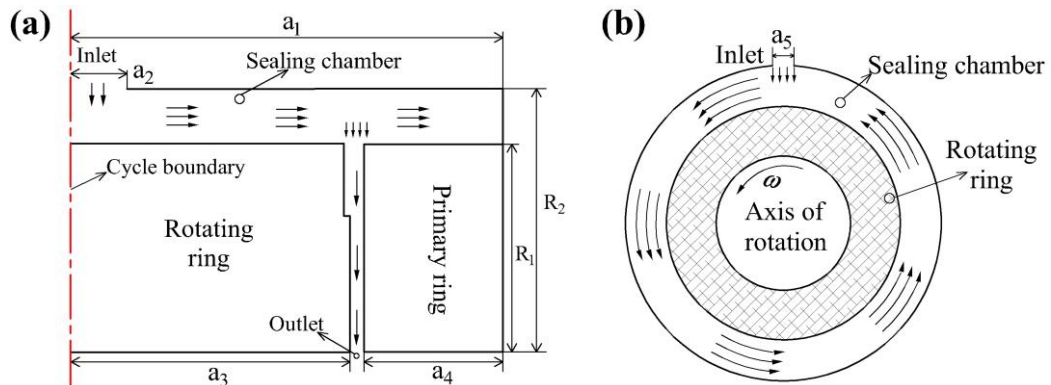


Fig. 2. Physical model of sealing chamber. (a) Axial. (b) Circumferential.

where ρ is the gas density and u_i ($i = 1, 2, 3$) is the velocity component in X, Y or Z direction. The compressible gas momentum conservation equation in a three-dimensional Cartesian coordinate system is written as follows:

$$\frac{\partial}{\partial x_i}(\rho u_i u_j) = -\frac{\partial p}{\partial x_j} - \frac{\partial}{\partial x_i} \left(\frac{2}{3} \mu \frac{\partial u_i}{\partial x_j} \right) + \frac{\partial}{\partial x_i} \left[\mu \left(\frac{\partial u_i}{\partial x_j} + \frac{\partial u_j}{\partial x_i} \right) \right] \quad (2)$$

where μ is the gas viscosity and p is the steady-state pressure. According to the basic law of energy conservation, all fluid systems undergoing heat transfer must satisfy the equation as follows:

$$\frac{\partial}{\partial x_i}(\rho u_i T) = \frac{\partial}{\partial x_i} \left(\frac{\kappa}{c_p} \text{grad} T \right) + S_T \quad (3)$$

where $\text{grad} T$ is gas temperature gradient, c_p is the

heat capacity at constant pressure of gas, κ is thermal conductivity, and S_T is thermal energy converted in viscous shear.

2.4 Theoretical Background of the Real Gas Effect

The RGE commonly refers to the performance of the pressure-specific volume-temperature relationship of the gas deviating from the ideal gas state equation. Generally, the RGE is expressed by the real gas state equation or compression factor Z_f . Many state equations of real gas describe the CO_2 . The Van der Waals equation, the RK equation, the Soave Redlich Kwong equation and the Peng Robinson equation (Feng *et al.* 2009) are compared with the National Institute of Standards and Technology (NIST) database, the RK equation is

the closest. The RK equation has the following form :

$$p = \frac{RT}{V-b} - \frac{a}{T^{0.5}V(V+b)} \quad (4)$$

The gas state equation can be written as follows:

$$pV = Z_f RT \quad (5)$$

Solving (4) and (5) simultaneously yields the real gas compression factor:

$$z_f = \left[-\frac{N}{2} + \sqrt{\left(\frac{N}{2}\right)^2 + \left(\frac{M}{3}\right)^3} \right]^{\frac{1}{3}} + \left[-\frac{N}{2} - \sqrt{\left(\frac{N}{2}\right)^2 + \left(\frac{M}{3}\right)^3} \right]^{\frac{1}{3}} + \frac{1}{3} \quad (6)$$

with M and N defined as follows:

$$M = -\left(\frac{1}{3} + \frac{p^2 b^2}{R^2 T^2} - \frac{ap}{R^2 T^{2.5}} + \frac{bp}{RT} \right)$$

$$N = -\frac{2}{27} - \frac{1}{3} \left(\frac{p^2 b^2}{R^2 T^2} - \frac{ap}{R^2 T^{2.5}} + \frac{bp}{RT} \right) - \frac{abp^2}{R^3 T^{3.5}}$$

Using (4)-(6), together with M and N , the density of the real gas is obtained:

$$\rho = \frac{pM}{RTz_f}$$

$$= \frac{pM}{RT \left\{ \left[-\frac{N}{2} + \sqrt{\left(\frac{N}{2}\right)^2 + \left(\frac{M}{3}\right)^3} \right]^{\frac{1}{3}} + \left[-\frac{N}{2} - \sqrt{\left(\frac{N}{2}\right)^2 + \left(\frac{M}{3}\right)^3} \right]^{\frac{1}{3}} + \frac{1}{3} \right\}} \quad (7)$$

The parameters a and b in the RK equation are defined as follows:

$$a = \frac{0.42748R^2 T_c^{2.5}}{P_c T_c^{0.5}} \quad b = \frac{0.08664RT_c}{P_c}$$

where R is gas constant, T is gas temperature, V is gas molar volume, and P_c and T_c are the critical pressure and critical temperature, respectively.

In addition to the gas density, the heat capacity at constant pressure c_p , viscosity μ , and thermal conductivity κ of the gas are also significantly affected by temperature, and therefore, these parameters need to be accurately expressed to consider the RGE (Yaws and Braker 2001):

$$c_p = 20.461 + 1.2299 \times 10^{-1} T - 1.6184 \times 10^{-4} T^2 + 1.0199 \times 10^{-7} T^3 - 2.4444 \times 10^{-11} T^4 \quad (8)$$

$$\mu = 11.336 \times 10^{-6} + 4.9918 \times 10^{-8} T - 1.0876 \times 10^{-11} T^2 \quad (9)$$

$$\kappa = -0.01183 + 1.0174 \times 10^{-4} T - 2.2242 \times 10^{-8} T^2 \quad (10)$$

2.5 The Theory of Heat Transfer

A fluid-structure coupled heat transfer occur in the gas of the sealing chamber, the gas film of the end face, the seal rings, and the sealing chamber, and

the formula for calculating the convective heat transfer coefficient (Jiao and Deng 2013) is as follows:

$$h_t = \frac{N_u \kappa}{r_o} \quad (11)$$

The Nusselt number is a quasi-number that indicates the intensity of convective heat transfer, and it is the ratio of the thermal resistance of the fluid layer to the thermal resistance of convective heat transfer. The Nusselt number can be expressed as follows:

$$N_u = 0.675 Re^{\frac{1}{2}} \quad (12)$$

Reynolds number (Kang *et al.* 2018) is a dimensionless quantity to predict the flow pattern in fluid mechanics. In the present study, Reynolds number is needed to solve N_u , and it can be expressed as follows:

$$Re = \frac{\rho v d}{\mu} \quad (13)$$

where the v is the linear speed of rotation and d is the characteristic length.

3. GRID MESHING AND MODEL VALIDATION

3.1 Grid Meshing

Cross-scale meshing is a challenge in this study since one must ensure that the grid sizes of the sealing chamber and gas film are in the similar order. Figure 3 (a) illustrates this model. The spiral groove of the gas film is measured in micrometers. It is difficult to observe under actual conditions, so the gas film enlarged by a factor of 1,000 along the Z direction to facilitate observation.

The whole model is enlarged 200 times in the axial direction, and then it is divided into four parts, (i.e., the gas film of the end face, the intermediate part between the gas film and the sealing chamber with the thickness the same as the gas film, and the gas in the sealing chambers A and B). The split surface of the model is created as the interface. The two sealing chambers are separated by the thickness of the gas film, and their dimensions are relatively large and regular. In order to merge the interface surface, the quadrilateral mesh type is used for division, and then the surface mesh is stretched along the axial direction to form an unstructured hexahedral mesh. Due to the sharp angle of the spiral grooves on the gas film, the grid on the surface must be denser. The grid type of the sealing chamber and gas film are shown in Fig. 3 (b) and (c). The intermediate area between the gas film and the sealing chamber primarily ensures that the grid sizes of the three parts are in the same order, and therefore, the aspect ratio of the grids can be guaranteed and the number of the grids can be reduced. The size ratio of the meshes of the three parts (i.e., the sealing chamber A and B, the intermediate part between the gas film and the

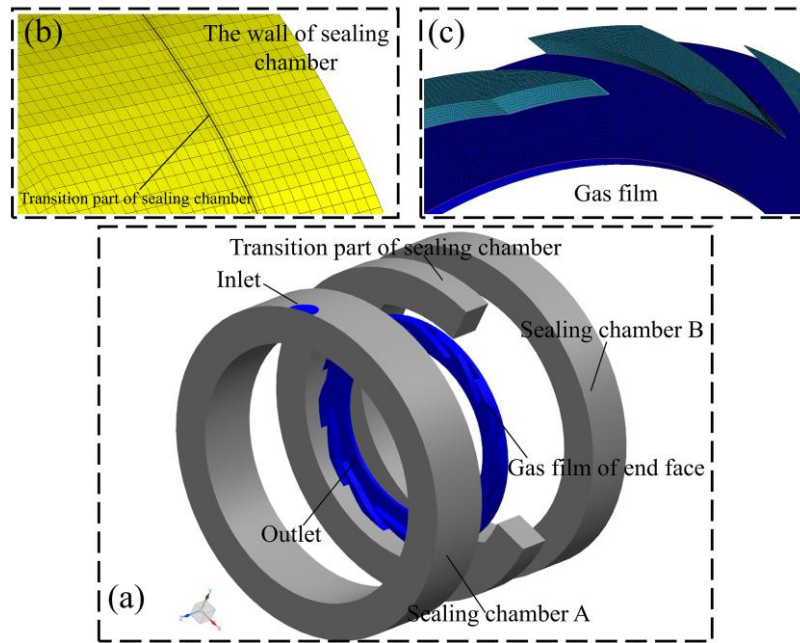


Fig. 3. Computational zones and boundary conditions.

sealing chamber, and the gas film) is set to 3: 1.5: 1. Finally, the three parts are ensembled through the interface in ICM software.

The density of mesh is tested to obtain a grid-independent solution. Five different meshes, from coarse to fine (i.e., with 4.27×10^6 , 6.31×10^6 , 9.31×10^6 , 1.02×10^7 , 1.51×10^7 grids), were generated. The results of the maximum pressure p_g of the groove on the end face and the total flow Q of the sealing chamber inlet were analyzed and compared. When the error of the results obtained under different grid numbers is less than 2% (Peng *et al.* 1996), the mesh can then be considered as ideal. Balancing the calculation accuracy and the computer configuration, the number of grids adopted in this study is 9.31×10^6 .

3.2 Boundary and Operating Parameters

The commercial software Fluent is used for the simulation. The sealing chamber and the gas film form a cross-scale flow field. Therefore, to obtain higher accuracy gas flow parameters, a shear stress transport (SST) $k-\omega$ model (Wang *et al.* 2013; Merati *et al.* 2001; Luan and Khonsari 2007; Joachimiak and Krzyślak 2019) with low Reynolds number method is used to calculate the near-wall region. However, the (SST) $k-\omega$ model requires very a small mesh of scale in the direction normal to the wetted wall, so the mesh is refined. The Real-gas-Redlich-Kwong model is selected for fluid material properties. The discreteness of density, momentum, and energy are all set to second-order upwind. And the convergency absolute accuracy of the model is set to 10^{-5} .

The gas inlet of the sealing chamber is set as the boundary condition of the pressure inlet with given

gas temperature T_0 . The inner side of the gas film is set as boundary condition of the out pressure, and the temperature is maintained at the default value of 300 K. Heat generated by the viscous shear of gas is mainly transferred to the surface of the sealing chamber, the rotating ring, and primary ring. Therefore, it is necessary to set the convective heat transfer boundary conditions and specify the convective heat transfer coefficient h_t .

In order to express the RGE of CO₂, the relative difference of the total mass flow at the sealing chamber inlet is defined:

$$E_1 = \frac{(Q_{real} - Q_{ideal})}{Q_{real}} \times 100\% \quad (14)$$

where Q_{real} is the total mass flow at the sealing chamber inlet of the real gas, and Q_{ideal} is the total mass flow at the sealing chamber inlet of the ideal gas.

3.3 Validation of Numerical Model

The RGE is mainly achieved by the gas compression factor expressing density. Therefore, the density values of gas in the RK model and the NIST database under different temperature and pressure conditions are selected and shown in Fig. 4(a). As indicated in this figure, the values obtained from the RK model match those in the NIST database since the error is less than 2%. The radial average pressure distribution of the gas film is compared with those in literature (Du *et al.* 2018; Wang *et al.* 2013; Song 2007), and the structure parameters are given in Table 1. Moreover, Fig. 4 (b) illustrates the results, which indicate that the results of this research are consistent with other studies.

Table 1 Structure parameters of the model

Parameter (unit)	Value	Parameter (unit)	Value
Sealing chamber axial length a_1 (mm)	30	Number of spiral groove N_g	12
Sealing chamber outer radius R_2 (mm)	88.78	Spiral depth h_g (μm)	5
Sealing chamber inlet radius a_2 (mm)	5	Spiral angle a ($^\circ$)	15
Seal ring outer radius r_o (mm)	77.78	Land-to-groove ratio g	1
Seal ring groove inner dam radius r_g (mm)	69	Shaft rotation speed n ($\text{r}\cdot\text{min}^{-1}$)	0-20000
Seal ring inner radius r_i (mm)	58.42	Inlet pressure p_i (MPa)	0.3-10.3
Gas film thickness h (μm)	2.03	Outlet pressure p_o (MPa)	0.1013
Rotating ring thickness a_3 (mm)	20	Inlet temperature T_i (K)	293.15-373.15
Mating ring thickness a_4 (mm)	10	Outlet temperature T_o (K)	300

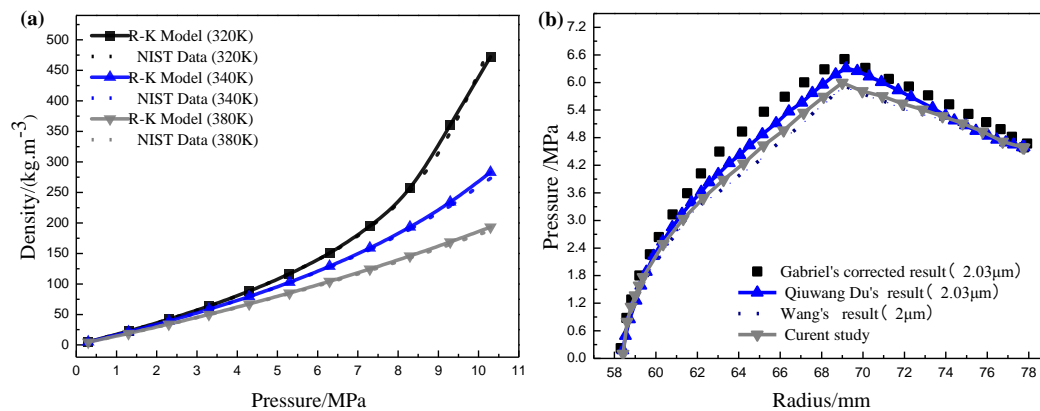


Fig. 4. Validation of the developed model (a) The density of R-K model compares with NIST database. (b)The pressure on the edge of groove ridge compares with reference.

4. RESULTS AND DISCUSSION

The structural parameters of the double-face S-DGS in the sealing chamber and end face are presented in Table 1 (Song 2007; Gabriel 1994; Ji *et al.* 2017; Chen *et al.* 2015).

4.1 Total Flow at the Sealing Chamber Inlet

Figure 5 shows the total flow change of the sealing chamber inlet under different working conditions, including the CO₂ real gas model, the ideal gas model, and the incompressible gas model. Results show that the total mass flows of three models increase with increasing pressure, and the total flow of the real gas model is greater than that of the ideal gas model and the incompressible gas model. The difference is particularly noticeable under high pressure. When the pressure reaches 10.3 MPa, the relative difference E_I is 51.90%, because the real gas equation (RK equation) can reflect the relationship between gas pressure and density or specific volume.

The real gas compression factor of CO₂ is less than 1, and its deviation from 1 increases at higher pressure. Therefore, it becomes easier to compress the real gas than it is to compress the ideal gas with

increasing pressure, which results in the total flow of real gas at the sealing chamber inlet being greater than the ideal gas. The total flows of real gas and ideal gas decrease with increasing temperature because the viscosity increases with increasing temperature. The average value of E_I is 2.18%. In the case of the total flow at the sealing chamber inlet, the effect of pressure is more significant than the effect of temperature. For the incompressible gas model, the total flow is significantly less than that of the real gas and the ideal gas at high pressure. Therefore, this model is only suitable at low pressure.

4.2 Analysis of Gas Flow in the Sealing Chamber and the End Face

In this section, the holistic characteristics of the sealing chamber and the gas film under different rotation speeds are analyzed. The gas film thickness, inlet pressure and inlet temperature are 2.03 μm , 4.5852 MPa, and 303.15 K, respectively, and the other parameters are given in Table 1.

4.2.1 Analysis of Pressures in the Sealing Chamber and the Gas Film

Figure 6 (a) presents the pressure change of the

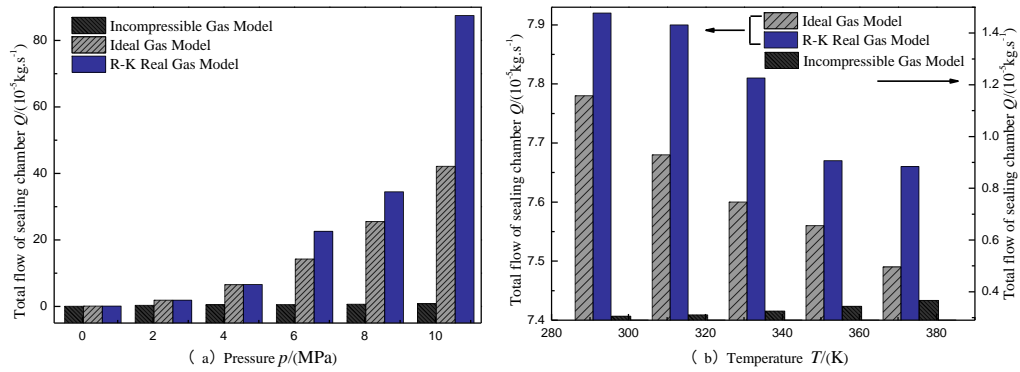


Fig. 5. Total flow of the sealing chamber under different operating conditions. (a) Pressure. (b) Temperature.

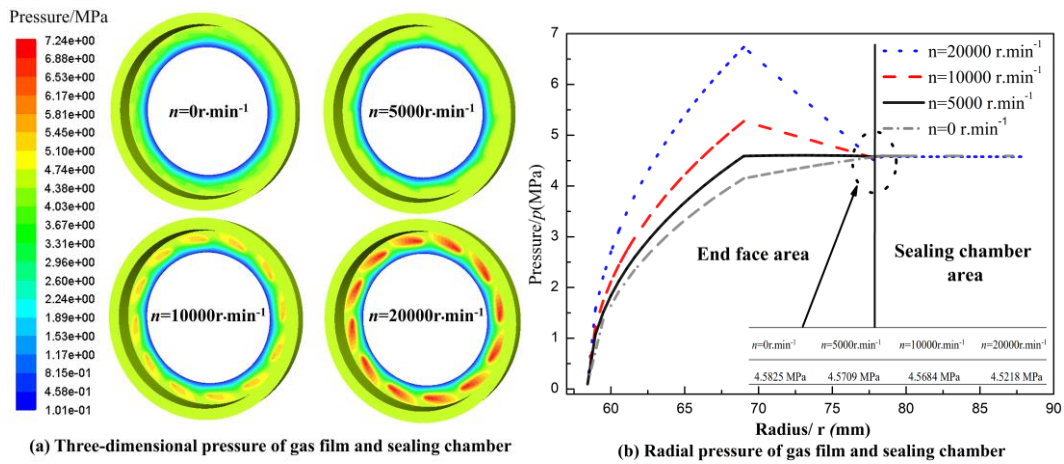


Fig. 6. Pressure distribution of gas film and sealing chamber.

sealing chamber and the gas film. The pressure change of the gas film is significant, ranging from 0.1 MPa to 7.24MPa with increasing rotation speed, and the maximum pressure appears at the groove root. The dynamic effect is caused by the sealing-ring rotation, and the pressure increases with the increase of the rotation speed. The pressure of the sealing chamber is relatively stable, and it tends to be consistent with the pressure at the sealing chamber inlet.

The radial pressure distribution of the sealing chamber and the gas film at different rotation speeds are illustrated in Fig. 6 (b). The minimum pressure in the sealing chamber occurs at the gas film inlet. The p_f is 4.5825MPa when the rotation speed is 0 $\text{r}\cdot\text{min}^{-1}$, and it decreases to 4.5218 MPa when the rotation speed is 20000 $\text{r}\cdot\text{min}^{-1}$. Therefore, when the gas flows from the millimeter-sized sealing chamber to the micron-sized gas film, the velocity and direction of gas flow change sharply at the end-face inlet, which cause additional gas friction and consume more energy. As a result, the local pressure loss occurs at the end face inlet. As the rotation speed increases, the pressure difference at the gas film increases, and the gas inlet velocity and outlet velocity also increase. The frictional energy consumption increases according to the changes of gas flow velocity and direction, which in turn leads to an increase of pressure drop at the gas

film inlet. However, the pressure drop at the gas film inlet is weak when the gas film thickness is 2.03 μm . Compared with the pressure at the sealing chamber inlet, the pressure decreases by 1.38% when the rotation speed reaches 20000 $\text{r}\cdot\text{min}^{-1}$.

4.22 Analysis of Temperature in the Sealing Chamber and the Gas Film

The temperature change of the sealing chamber and the gas film is presented in Fig. 7 (a). It can be seen that the temperature changes from 300 K to 711K. The high-temperature region appears in the gas film and it changes significantly. The temperature of the sealing chamber is uniformly distributed, and it is close to the temperature at the sealing chamber inlet, because the main heat source of DGS is the viscous shear of the gas through the rotation of the rotating ring. Since the gas film of the end face is on the micrometer scale, the viscous shear heat is significant, which leads to high temperature. However, the size of the sealing chamber is much larger, but the viscous shear heat of the gas is not significant. Figure 7 (b) illustrates the temperature distributions of the sealing chamber and the gas film along the radial at different rotation speeds. The gas film thickness in the groove area is larger than that in the land area and the dam area, so the temperature is lower in the groove area. The spiral groove is the main reason for the dramatic change

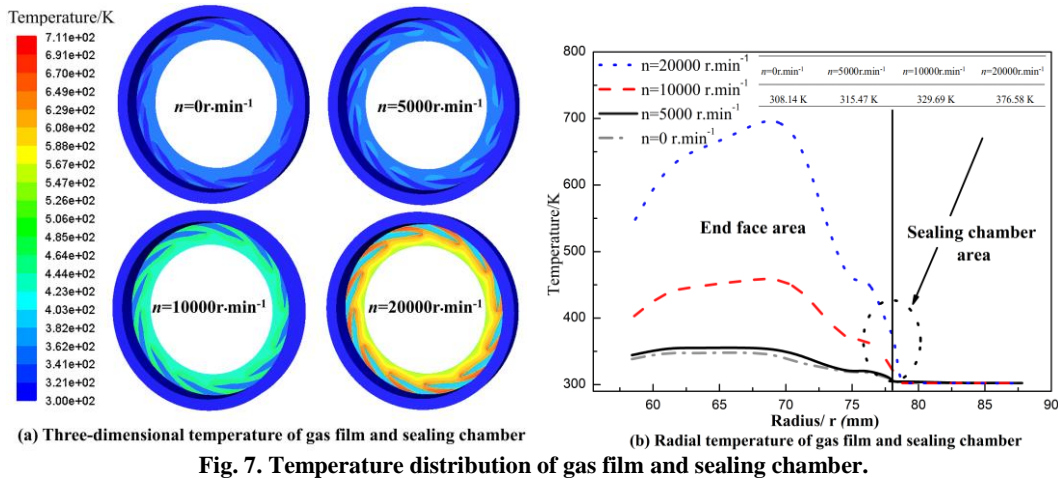


Fig. 7. Temperature distribution of gas film and sealing chamber.

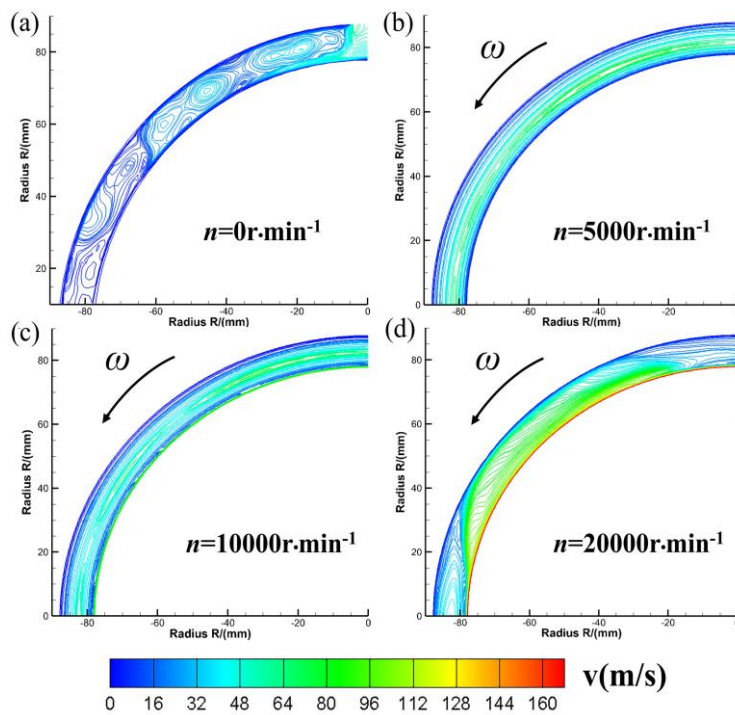


Fig. 8. Circumferential gas flow contour map of sealing chamber at different rotation speeds.

in the temperature curve. However, the change in temperature of the sealing chamber is Minor, and the maximum temperature of the sealing chamber appears at the gas film inlet. T_f is 308.14K when the rotation speed is 0 r.min⁻¹, and it increases as the rotation speed increases. T_f is 376.58K when the rotation speed is 20000 r.min⁻¹, and the temperature is increased by 19.50% compared to the temperature at the sealing chamber inlet. In summary, the results presented in Fig. 6 and Fig. 7 indicate that the temperature and pressure of the sealing chamber do not change significantly with the rotation speed, and they are close to those in the sealing chamber inlet. However, the rotation speed has a significant effect on the temperature and pressure at the gas film inlet.

4.23 Analysis of Sealing Chamber flow Velocity

Figure 8 presents the circumferential flows of the sealing chamber in the inlet at different rotation speeds. The circumferential section in the sealing chamber is small and the streamlines are dense. A quarter of the circumferential section is selected and enlarged. Many vortex flow regions are present in the sealing chamber when the rotation speed is 0 r.min⁻¹, and maximum flow velocity occurs at the sealing chamber inlet. The sealing chamber can be regarded as a row of casing when the gas flows in it. When the gas flows in the sealing chamber, the gas circumferential flow and the gas axial flow are superimposed. With the increase of the rotation speed, the gas is forced to flow by the viscous

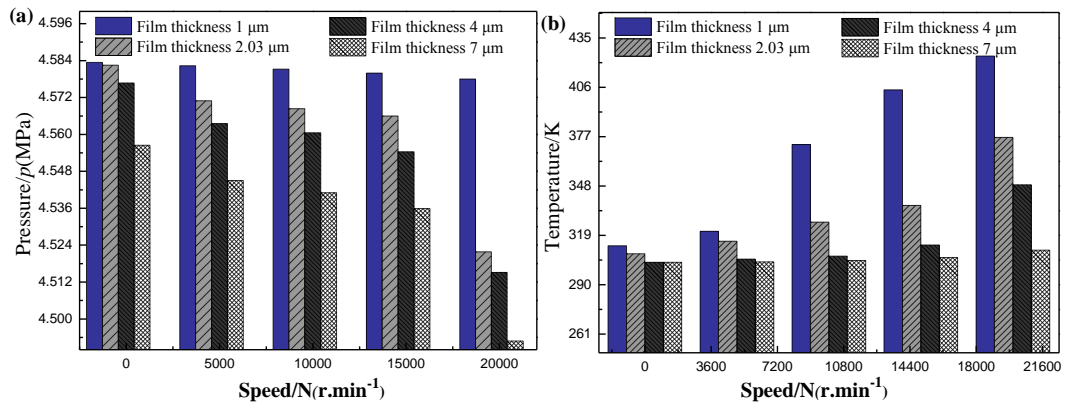


Fig. 9. The change of end face inlet at different speed (a) Pressure. (b) Temperature.

Table 2 The factors and levels of the RSM test for sealing chamber and gas film

Code	Factor (unit)	Level 1	Level2	Level 3	Level 4	Level 5
		-2	-1	0	1	2
A	Shaft rotation speed n (r.min ⁻¹)	0	5000	10000	15000	20000
B	Gas film thickness h (μm)	1	6	11	16	21
C	Inlet pressure of sealing chamber p_i (MPa)	0.3	2.8	5.3	7.8	10.3
D	Inlet temperature of sealing chamber T_i (K)	293.15	313.15	333.15	353.15	373.15

shearing, and the free flow reduces, which leads to reduction of the vortex region. The gas circumferential velocity in the sealing chamber increases as the rotation speed increases. The velocity contour near the outer surface of the seal ring is dense, and the velocity is substantial.

When the rotation speed reaches 20000 r.min⁻¹, the gas in the sealing chamber is driven by the rotating ring, and the circumferential velocity continues to increase. However, there is continuous gas inflow at the sealing chamber inlet and the flow velocity is low. Therefore, the circumferential flow velocity at the sealing chamber inlet is smaller than that of the gas in the sealing chamber. The current conclusion is based on the theory of fluid mechanics and is situated in the macroscopic scope. For the microstructure, the flow and heat transfer of molecules in the fluid are complicated and different. It needs to be analyzed by fractal calculus theory (Ain and He 2019; He and Ji 2019; He and Ain 2020), which is the focus of a future study.

4.3 Effect of Sealing Chamber on Inlet Pressure and Inlet Temperature of Gas Film

Figure 9 presents the variation characteristics of p_f and T_f at different rotation speeds. This figure demonstrates that the p_f decreases with the increase of the rotation speed. Furthermore, the larger the film thickness, the smaller the p_f . This is because increasing the rotation speed and the film thickness will increase the flow at the gas film inlet. More gases undergo dramatic changes in their flow velocity and direction, which causes friction to consume energy and reduce pressure.

When $n = 20000$ r.min⁻¹, $h = 7\mu\text{m}$, the p_f is

4.49MPa, which is a decrease of 2.02% compared to the inlet pressure of the sealing chamber. However, the effects of film thickness and rotation speed on T_f are opposite. As the rotation speed increases, the viscous shear increases, which leads to temperature increase of the gas film and gas film inlet. As the film thickness increases, the gas film flow velocity increases, and more low-temperature CO₂ gas enters the gas film inlet, which results in the temperature decrease. When $n = 20000$ r.min⁻¹ and $h = 1\mu\text{m}$, the T_f is 424.38K, which is 1.40 times the one in the sealing chamber inlet. The change of T_f at the gas film inlet is significant, and its value cannot be ignored. To summarize, the temperature change of the gas film inlet should be considered when the gas film is thin, and the pressure change of the gas film inlet should be considered when the gas film becomes thicker.

The above analyses indicate that the gas flow in the sealing chamber affects T_f and p_f . Moreover, the main influencing factors are the temperature and pressure of the sealing chamber inlet, the rotation speed, and the gas film thickness. To further explore the characteristics of the gas film inlet, multiple regression analyses were performed using the response surface methodology with a central composite rotatable design (Peng *et al.* 2015; Yu *et al.* 2020; Fouladi and Czupryna 2018). The inlet temperature of the sealing chamber, the inlet pressure of the sealing chamber, rotation speed, and film thickness are selected for 5-level and 4-factor multiple regression analysis. The model setting is given Table 2. Table 3 presents the preliminary design and numerical results. Several regression models are compared through the characteristics of the current data. And a second-order polynomial model of the design (Eq. (15)) is employed to

Table 3 Detailed simulation scheme and results according to RSM

Parameter	A	B	C	D	Inlet pressure of end face p_f	Inlet temperature of end face T_f
1	0	0	0	0	4.8341	334.0621
2	1	-1	-1	1	2.7272	357.9692
3	-1	-1	-1	1	2.7552	351.7157
4	1	1	-1	-1	2.3945	315.7102
5	0	2	0	0	3.8880	323.0136
6	-1	1	1	1	6.6329	351.9654
7	-1	-1	1	1	7.6754	352.7638
8	1	-1	1	1	7.7570	354.5468
9	-1	1	1	-1	7.0909	311.9358
10	1	1	1	-1	6.5265	312.8431
11	0	0	0	0	4.2341	334.0621
12	0	0	0	0	4.8341	334.0621
13	-2	0	0	0	4.9216	332.5599
14	0	0	2	0	9.39521	333.5641
15	0	0	0	0	4.8341	334.0621
16	0	0	0	0	4.8341	334.0621
17	-1	-1	1	-1	7.6731	312.5168
18	0	-2	0	0	5.2954	417.1187
19	-1	1	-1	-1	2.7296	312.9573
20	1	-1	1	-1	7.5721	314.7658
21	-1	-1	-1	-1	2.7527	313.0379
22	0	0	0	2	4.8441	373.7622
23	-1	1	-1	1	2.4263	352.1719
24	1	-1	-1	-1	2.7247	318.8547
25	0	0	-2	0	0.2776	337.5418
26	0	0	0	0	4.8341	333.9112
27	1	1	-1	1	2.3981	354.4442
28	1	1	1	1	6.5662	353.8649
29	0	0	0	-2	4.8351	294.5900
30	2	0	0	0	4.8031	339.8899
31	0	0	0	0	4.8341	334.0621

evaluate the response variable as a function of the independent variables and their interactions.

$$Y = b_0 + \sum_{i=1}^4 (b_i X_i) + \sum_{i=1}^3 \sum_{j=i+1}^4 b_{ij} X_i X_j + \sum_{i=1}^4 (b_{ij} X_i^2) \quad (15)$$

The determination coefficient (R^2) given in Eq. (16) is used to compare and analyze the accuracy of the agent model.

$$R^2 = \frac{SS_{Model} \sum (\hat{y}_i - \bar{y})^2}{\sum (y_i - \bar{y})^2} = 1 - \frac{\sum (y_i - \bar{y})^2}{\sum (\hat{y}_i - \bar{y})^2} \quad (16)$$

where y_i is the response value of the i -th sample, \bar{y} is the mean value of the response sample, and \hat{y} is the predicted value of the polynomial

model in the i -th sample.

The coefficients of the second order RSM model of the T_f and p_f are shown in Table 4, where the P-value reflects the significance of parameter. The smaller the P-value, the higher the significance. The P-value in Table 4, it can be determined that the first order terms X_2 , X_3 , and the quadratic term X_2X_3 have a significant effect on p_f . In other words, the inlet pressure of the sealing chamber and the gas film thickness are important factors affecting the p_f , and the effects are greater than that of the rotation speed and inlet temperature of the sealing chamber. The first order term X_2 and X_4 and the second order terms X_2X_2 have a significant effect on T_f , indicating that the gas inlet temperature of the sealing chamber and film thickness are important factors affecting the T_f . In addition to the inlet temperature and inlet pressure of the sealing chamber, the film thickness

Table 4 Significance test of regression coefficient

p_f model term	Parameter estimate	Standard error	T value	P value	T_f model term	Parameter estimate	Standard error	T value	P value
Intercept (b_0)	4.74841	0.06349	74.668	0.000	Intercept (b_0)	334.041	5.464	61.139	0.000
X_1 (b_1)	-0.05444	0.03434	-1.585	0.132	X_1 (b_1)	1.608	2.951	0.545	0.593
X_2 (b_2)	-0.32029	0.03434	-9.326	0.000	X_2 (b_2)	-8.27	2.951	-2.803	0.013
X_3 (b_3)	2.28421	0.03434	66.509	0.000	X_3 (b_3)	-0.817	2.951	-0.277	0.785
X_4 (b_4)	-0.02116	0.03434	-0.616	0.547	X_4 (b_4)	19.799	2.951	6.710	0.000
$X_1 \times X_1$ (b_{11})	0.04809	0.03146	1.529	0.146	$X_1 \times X_1$ (b_{11})	-1.142	2.703	-0.422	0.678
$X_2 \times X_2$ (b_{22})	-0.01957	0.03146	-0.622	0.543	$X_2 \times X_2$ (b_{22})	7.319	2.703	2.707	0.016
$X_3 \times X_3$ (b_{33})	0.04160	0.03146	1.322	0.205	$X_3 \times X_3$ (b_{33})	-1.310	2.703	-0.484	0.635
$X_4 \times X_4$ (b_{44})	0.04240	0.03146	1.348	0.197	$X_4 \times X_4$ (b_{44})	-1.654	2.703	-0.612	0.549
$X_1 \times X_2$ (b_{12})	-0.05743	0.04206	-1.365	0.191	$X_1 \times X_2$ (b_{12})	-0.517	3.614	-0.143	0.888
$X_1 \times X_3$ (b_{13})	-0.01446	0.04206	-0.344	0.735	$X_1 \times X_3$ (b_{13})	-0.641	3.614	-0.177	0.861
$X_1 \times X_4$ (b_{14})	0.06169	0.04206	1.467	0.162	$X_1 \times X_4$ (b_{14})	0.03	3.614	0.008	0.993
$X_2 \times X_3$ (b_{23})	-0.17810	0.04206	-4.234	0.001	$X_2 \times X_3$ (b_{23})	0.144	3.614	0.04	0.969
$X_2 \times X_4$ (b_{24})	-0.05689	0.04206	-1.355	0.195	$X_2 \times X_4$ (b_{24})	0.074	3.614	0.02	0.984
$X_3 \times X_4$ (b_{34})	0.00397	0.04206	0.094	0.926	$X_3 \times X_4$ (b_{34})	0.334	3.614	0.092	0.928
$R^2=0.9965$					$R^2=0.7956$				

has significant effect on the p_f and T_f , and the impact is greater than that of the rotation speed. As the film thickness increases, both the p_f and T_f decrease. Table 4 shows that the second order RSM model for pressure has a higher degree of fitting. However, the R^2 of T_f is lower than the R^2 of p_f , because non-linear factors can affect the T_f . These factors include the changes in viscous shear force due to rotation speed, the changes in density due to pressure and temperature, the changes in viscosity with temperature, and heat transfer to the exterior. These factors are relatively complex and hence are not included in the RSM model.

5. CONCLUSION

Since the critical temperature and pressure of CO₂ are relatively low, it is easy to reach the critical state under common operating conditions, even in a supercritical state. The real gas behavior deviates significantly from the ideal gas, thereby affecting the sealing performance. In this paper, the RGE of CO₂ is expressed by the RK equation. The physical parameters of CO₂ during DGS operation is considered throughout the process. Taking double-face S-DGS as the research object, the cross-scale model of the sealing chamber and the gas film, as well as the simulation is built using CFD commodity software. The changes of flow characteristics such as temperature, pressure, flow rate of sealing chamber gas with different working conditions, and the influence of the sealing chamber on the end-face inlet are analyzed.

A method for analyzing the cross-scale flow field under the RGE of CO₂ is provided by using the double-face S-DGS as an example. The total gas flow at the sealing chamber inlet increases with increasing pressure. However, it decreases with increasing temperature. When the working pressure reaches 10.3 MPa, the relative difference E_1 is 51.90%, and the average relative difference E_1 is 2.18% when the temperature is within 293.15K to 373.15K.

Many vortex flow areas occur in the sealing chamber when the rotation speed is 0 r.min⁻¹, because the gas circumferential flow superimposes the gas axial flow in the sealing chamber. When the rotation speed increases, the gas is driven by the rotating ring. Therefore, the vortex flow areas reduce. There is still a vortex flow area above the end-face inlet. The changes of temperature and pressure in the sealing chamber are not significant when the DGS is in operation, but T_f increases and p_f decreases at the sealing chamber inlet.

Furthermore, a multiple regression analysis determined that the inlet temperature of the sealing chamber, the inlet pressure of the sealing chamber, and the gas film thickness of the end face have a significant effect on T_f and p_f .

ACKNOWLEDGEMENTS

The authors gratefully acknowledge support by the National Nature Science Foundation of China (No. 51465026), and Analysis and Testing Foundation of

Kunming University of Science and Technology (granted no. 2019P20173103005)

REFERENCES

- Ain, Q. and J. He (2019). On two-scale dimension and its applications. *Thermal Science* 23 (3), 1707–1712.
- Chen, D., X. Ding, S. Yu and W. Zhang (2019). Friction performance of DLC film textured surface of high pressure dry gas sealing ring. *Journal of the Brazilian Society of Mechanical Sciences and Engineering* 41(161), 2-8.
- Chen, H., Z. Liu, T. Liu, B. Zhao and S. Li (2015). Research on coupling style of mechanical seal with spiral groove and micro-pores based on cavitation. *Journal of Jiangsu University (Natural Science Edition)* 36(1), 43-47.
- Chen, Y., X. Peng, J. Jiang, X. Meng and J. Li (2018). Experimental and theoretical studies of the dynamic behavior of a spiral groove dry gas seal at high-speeds. *Tribology International* 125, 17-26.
- Du, Q., K. Gao, D. Zhang and Y. Xie (2018). Effects of grooved ring rotation and working fluid on the performance of dry gas seal. *International Journal of Heat and Mass Transfer* 126, 1323-1332.
- Du, Q., L. Zhang, D. Zhang and Y. Xie (2020). Numerical investigation on flow characteristics and aerodynamic performance of shroud seal in a supercritical CO₂ axial-flow turbine. *Applied Thermal Engineering* 169(25), 114960.
- Fairuz, Z. and I. Jahn (2016). The influence of real gas effects on the performance of supercritical CO₂ dry gas seals. *Tribology International* 102, 333-347.
- Fairuz, Z., I. Jahn and R. Abdul-Rahman (2019). The effect of convection area on the deformation of dry gas seal operating with supercritical CO₂. *Tribology International* 137, 349-365.
- Feng, X., A. Xuan and C. Zhou (2009). *Chemical Thermodynamics*. Beijing, Publishing House of Chemical Industry Press.
- Fouladi, K. and J. Czupryna (2018). CFD-Based Optimization of Micro Vortex Diodes. *Journal of Applied Fluid Mechanics* 11 (5), 1231-1237.
- Gabriel, R. (1994). Fundamentals of Spiral Groove Noncontacting face Seals. *Lubrication Engineering* 50(3), 215-224.
- He, J. and F. Ji (2019). two-scale mathematics and fractional calculus for thermodynamics. *Thermal Science* 23 (4), 2131–2133.
- He, J. and Q. Ain (2020). New promises and future challenges of fractal calculus From Two-Scale Thermodynamics to Fractal Variational Principle. *Thermal Science* 24 (2), 659–681.
- Ji, H., X. Chen, Y. Wang, K. Zhang and Z. Chen (2017). Outlet suction and leakage of mechanical seal with inclined elliptical dimples. *Advanced Engineering Sciences* 49(2), 248-253.
- Jiao, F. and X. Deng (2013). Structural optimization of converging-diverging tube based on heat transfer enhancement for self-support rectangle heat exchanger. *CIESC Journal* 64(7), 2376-2385.
- Joachimiak, D. and P. Krzyślak (2019). Analysis of the Gas Flow in a Labyrinth Seal of Variable Pitch. *Journal of Applied Fluid Mechanics* 12 (3), 921-930.
- Kang, Y., M. Liu, S. Kao-Walter, W. Rehemann and J. Liu (2018). Predicting aerodynamic resistance of brush seals using computational fluid dynamics and a 2-D tube banks model. *Tribology International* 126, 9 -15.
- Li, Q. (2007). *Numerical Simulation Analysis and Optimal Design of DGS on Spiral Groove End*. Master. thesis, the East China University of Science and Technology, Shanghai, China.
- Luan, Z. and M. Khonsari (2007). Computational Fluid Dynamics Analysis of Turbulent Flow Within a Mechanical Seal Chamber. *Tribology of the ASEME* 129(4), 120-128.
- Meng, X. and M. khonsari (2018). Viscosity Wedge Effect of Dimpled Surfaces Considering Cavitation Effect. *Tribology International* 122, 58-66.
- Merati, P., J. Payva and R. Phillips (2001). Effect of Impeller Geometry, Rotation Speed, and Fluid Properties on Seal Chamber Flow. *Tribology Transactions* 44(3), 451-457.
- Peng, L., X. Gao and K. Chen (2015). Catalytic upgrading of renewable furfuryl alcohol to alkyl levulinates using AlCl₃ as a facile, efficient, and reusable catalyst. *Fuel* 160, 123-131.
- Peng, X., Y. Xie and Y. Gu (1996). Determination of the end faces temperature of mechanical seal, *Chem. Eng. Mach* 23(6), 33-336.
- Song, P. (2007). Discussion on calculation method of gas film pressure on spiral groove dry gas end face. *Lubrication Engineering* 34 (7), 7-17.
- Song, P. and Z. Ding (2011). An approximate analytical method of the gas film pressure of the outward pumping spiral groove dry gas seals. *Lubrication Engineering* 36(4), 1-3.
- Thatte, A. and V. Dheeradhada (2016, September). Coupled Physics Performance Predictions and Risk Assessment for Dry Gas Seal Operating in MW-Scale Supercritical CO₂ Turbine. In *Turbomachinery Technical Conference and Exposition*, Seoul, South Korea.
- Wang, F. (2004). *Dynamics Analysis of Computational Fluid and Applications of CFD*

- Software*. Beijing, Publishing House of Tsinghua University Press.
- Wang, H., B. Zhu, J. Lin and C. Ye (2013). A Thermohydrodynamic Analysis of Dry Gas Seals for High-Temperature Gas-Cooled Reactor. *Journal of Tribology* 135, 021701.1-021701.9.
- Wang, Y., J. Sun, Q. Hu, D. Wang and X. Zheng (2018). Orientation effect of orderly roughness microstructure on spiral groove dry gas seal. *Tribology International* 126, 97-105.
- Wang, Y., Q. Hu, J. Sun, D. Wang and X. Zheng (2019). Numerical analysis of T-groove dry gas seal with orientation texture at the groove bottom. *Advances in Mechanical Engineering* 11 (1), 1-12.
- Xie, J., C. Ma and S. Bai (2020). Thermo-distortion characteristics of spiral groove gas face seal at high temperature. *Numerical Heat Transfer, Part B: Fundamentals* 77(3), 242-256.
- Xu, H., P. Song, W. Mao and Q. Deng (2019). The performance of spiral groove drygas seal under choked flow condition considering the real gas effect. *Proceedings of the Institution of Mechanical Engineers, Part J: Journal of Engineering Tribology* 234(4), 554-566.
- Xu, H., P. Song, W. Mao, Q. Deng and X. Sun (2018). Analysis on inertia effect of carbon dioxide dry gas seal at high speed and pressure under laminar condition. *CIESC Journal* 69(10), 4311-4323.
- Yaws, C. and W. Braker (2001). *Matheson gas data book*. New York, Publishing House of McGraw-Hill.2001.
- Yu, C., H. Zhang, M. Zeng, R. Wang and B. Gao (2020). Numerical study on turbulent heat transfer performance of a new compound parallel flow shell and tube heat exchanger with longitudinal vortex. *Applied Thermal Engineering* 160, 114449.